Research Square

Preprints are preliminary reports that have not undergone peer review.
They should not be considered conclusive, used to inform clinical practice,
or referenced by the media as validated information.

Intermodal coupling and Bright-Dark Solitons in Concentric Micro-Ring Comb Generators

Nabil Emara

nabil.emara@mail.utoronto.ca

Ain Shams University

Hussein Kotb

University of Toronto

Diaa Khalil

Ain Shams University

Research Article

Keywords:

Posted Date: August 3rd, 2026

DOI: https://doi.org/10.21203/rs.3.rs-10349698/v1

License: This work is licensed under a Creative Commons Attribution 4.0 International License.
Read Full License

Additional Declarations: No competing interests reported.

Intermodal coupling and Bright-Dark Solitons in Concentric Micro-Ring Comb Generators

Nabil Emara[1,2*], Hussein Kotb[1] and Diaa Khalil[1]

[1*]Faculty of Engineering, Ain-Shams University, 1 Elsarayat St., Abbassia, Cairo, Egypt.
[2]Edward S. Rogers Sr. Department of Electrical and Computer Engineering, University of Toronto, 35 St George St, Toronto, M5S 3G4, Ontario, Canada.

*Corresponding author(s). E-mail(s): nabil.emara@mail.utoronto.ca;

Abstract

Concentric micro-ring resonator optical frequency comb (OFC) generators provide a dispersion engineering technique to generate two supermodes with opposite signs of dispersion parameter in the wavelength region around $\mathbf{1.55\,\mu m}$ in silicon nitride waveguides. In this work, we report two designs of the concentric micro-ring resonator. Design 1 (2) has an anomalous dispersion region and a dispersion parameter peak value of **5000** and $\mathbf{1 \times 10^5}$ ps/nm.km, respectively. To the best of our knowledge, this is the first report for the impact of the intermodal coupling between the cavity supermodes at the location of the directional coupler on the frequency comb generation dynamics. We develop a modified Ikeda map with intermodal boundary conditions and investigate the system's modulation instability, demonstrating that concentric micro-ring resonators can support tri-stable CW states as well as co-propagating bright–dark solitons.

1 Introduction

Optical Frequency Combs (OFCs) have become a central focus of research for many research groups all over the world in the last few years [1]. Different techniques have been proposed for OFC generation; between these techniques, the mode-locked OFC can achieve an ultra-broad spectrum band, with very precise equidistant spectral lines conducive to a multitude of uses in metrology [2,3], frequency synthesis [4], optical clocks, spectroscopy [5], and dense wavelength division multiplexing (DWDM) [6].

Integrated micro resonator OFC provides the added benefit of scalability, tunability, and ease of manufacturing using the existing electronic integrated circuit (IC) technologies [7–9]. For DWDM, silicon nitride (Si_3N_4) is an excellent candidate due to its transparency in the telecom wavelengths, integrability with current IC technology, and high Kerr nonlinearity that is an order of magnitude larger than silica fibers. In addition, in contrast to silicon, Si_3N_4 has negligible two-photon absorption (TPA) due to its dielectric nature and large bandgap [10]. OFCs exhibit various rich dynamics and operational regimes including bistable and multi-stable continuous-wave (CW) states, Turing patterns, chaos, and perhaps the most desirable localized cavity solitons, which provide the most stable and correlated lines [11].

OFC generation depends on two main aspects:

1-Kerr nonlinearity, which exhibits effects proportional to the optical intensity, such as self-phase, cross-phase modulation, and four-wave mixing. High-quality factor micro-ring resonators can scale down the threshold optical intensity required for the generation of frequency combs [12–14].

2-Dispersion that plays an important role in the dynamics of OFCs and the nature of the solitons produced. Anomalous dispersion ($\beta_2 < 0$) is required for bright soliton generation [15–17], while normal dispersion ($\beta_2 > 0$) does support dark soliton generation [17]. Si_3N_4 waveguides with the dimensions commonly used in the market exhibit normal dispersion in the telecom wavelengths; however, some topologies have been proposed in the literature to achieve a flip in the dispersion sign for a certain frequency band via engineered modal interactions, such as concentric micro-rings [18] and coupled micro-rings [19]. OFC modelling reported in the literature is mostly based on the coupled mode equations [15] or the Lugiato–Lefever equation (LLE), when the variations in the gain and loss are low per round trip [20]. On the other hand, the full dynamics of the frequency comb are captured by the Ikeda map model [21–23], which we use here in our analysis. In this work, we focus on the analysis of concentric rings near the avoided mode crossing (AMC) point using the Ikeda map model. In section 2, we outline the methodology used for choosing the cavity dimensions for dispersion engineering. In section 3, we model novel phenomena of linear intermodal coupling due to the perturbations occurring at the coupling region and analyze its effect on the boundary conditions. Then, we obtain a modified temporal dynamics model of this system via a modified Ikeda map. In section 4, we model the CW response of our system, revealing tristable solutions and embedded intermodal peaks. In section 5, we model the modulation instability of our system and reveal how our perturbed system deviates from the classic behavior of such resonators. In section 6, we simulate our cavity using a detuning sweep, revealing that our cavity supports co-propagating Bright and Dark solitons. The paper ends with the conclusion.

2 Dispersion Engineering of the Micro-ring resonator

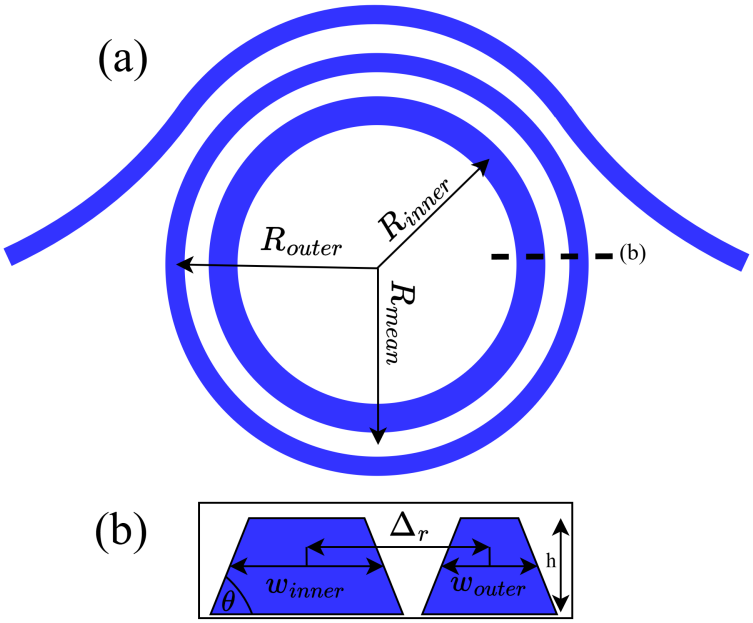


Fig. 1 (a) Schematic diagram of the concentric micro-ring showing the definitions of different radii, (b) cross-section of the waveguides at the point outlined in (a) showing the definitions of the widths, height, and Δ_r.

In this section, we introduce the theory and methodology used to achieve anomalous dispersion employing the AMC technique and present our modal simulation results. The schematic diagram of the considered concentric micro-ring resonator is shown in Fig. 1(a). The inner and outer rings are totally coupled with each other. We employed the Si_3N_4 waveguide structure shown in Fig. 1(b), which is compatible with Applied NanoTools (ANT) technology. The waveguide height is $h = 400\,\text{nm}$ and the side wall angle is $\theta = 83.5°$. The estimated attenuation coefficient is $1.3\,\text{dB/cm}$ for the bent waveguides. The optical path lengths (OPL) of the fundamental modes of each isolated ring are matched at the design wavelength such that:

$$\text{OPL} = 2\pi R n_{\text{eff}} \tag{1}$$

where R is the radius of each ring [Fig. 1(a)], and n_{eff} is the effective index of the fundamental mode of the bent waveguide. This matching condition causes the uncoupled modes to hybridize, and we then have two orthogonal supermodes (symmetric mode 1 and anti-symmetric mode 2) for this concentric micro-ring resonator, as illustrated in Fig. 4. Our design is targeting a dense wavelength division multiplexing frequency grid with 200 GHz frequency separation. The free spectral range (FSR) of a resonator

is given by [24]:

$$\mathrm{FSR} = \frac{c}{2\pi n_g R_{\mathrm{mean}}} \tag{2}$$

where R_{mean} is the mean radius between both rings:

$$R_{\mathrm{mean}} = \frac{R_{\mathrm{outer}} + R_{\mathrm{inner}}}{2} \tag{3}$$

n_g is computed to be 2.035 at the central wavelength (1.55 μm). Thus, we obtain $R_{\mathrm{mean}} = 117.23\,\mu$m. We then use Lumerical mode suite to sweep the OPL (at 1.55 μm) against the difference in radii, given as:

$$\Delta_r = R_{\mathrm{outer}} - R_{\mathrm{inner}} \tag{4}$$

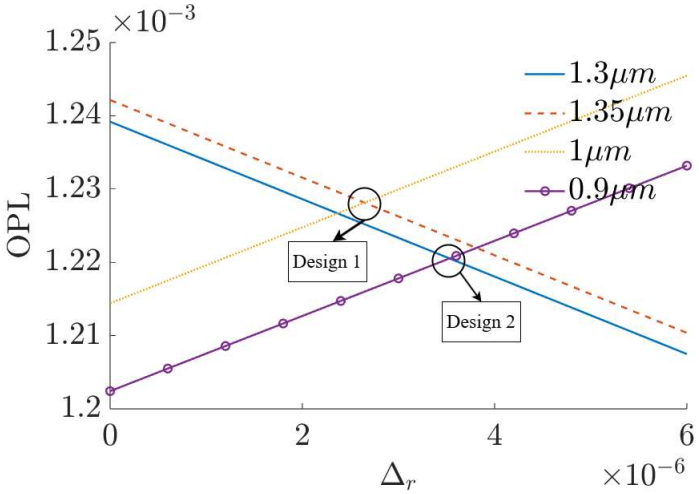


Fig. 2 Plot of OPL versus Δ_r for four different values of waveguide mean width. Two design points are mentioned in this figure and outlined in Table 1.

Whilst keeping R_{mean} constant as shown in Fig. 2, we choose outer waveguides of width $w_{\mathrm{outer}} = 1.0\,\mu$m and 0.9 μm, and for inner waveguides $w_{\mathrm{inner}} = 1.35\,\mu$m and 1.30 μm. This yields four possible designs at each intersection point, of which we restrict ourselves to the two cases outlined in Table 1.

Table 1 Dimensions for the two proposed designs

Design number	$w_{\mathrm{outer}}, w_{\mathrm{inner}}$ (μm)	Δ_r (μm)
1	1.0, 1.35	2.652
2	0.9, 1.30	3.534

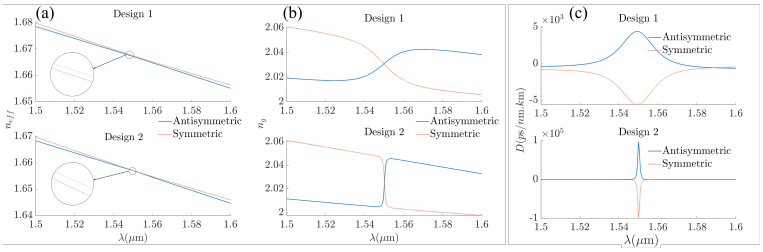


Fig. 3 (a) n_{eff} against wavelength for both designs, showing the AMC. Zooming in on the AMC point shows that the lines do not intersect. (b) n_g versus wavelength shows how the antisymmetric mode has a positive slope around 1.55 μm, which indicates anomalous dispersion. (c) The dispersion parameter clearly indicates positive values (anomalous dispersion) for the antisymmetric modes of both designs.

Figure 3(a) shows the change of the effective indices of the symmetric and asymmetric supermodes with wavelength. AMC is observed for both designs. Figure 3(b) shows the change in the group index with wavelength for the antisymmetric mode, which exhibits a positive slope in a certain wavelength span around the center wavelength of 1550 nm, indicating the anomalous dispersion region [24]. The size of that region and the magnitude of the slope change are shown in Fig. 3(c). This shows that as Δ_r increased, the magnitude of the anomalous dispersion peak increased, and the bandwidth of the anomalous region decreased; thus, the choice of widths is not very restrictive, as long as Δ_r is not too large so that the anomalous dispersion bandwidth does not cover multiple resonances or too small as to not give a flip in the dispersion sign.

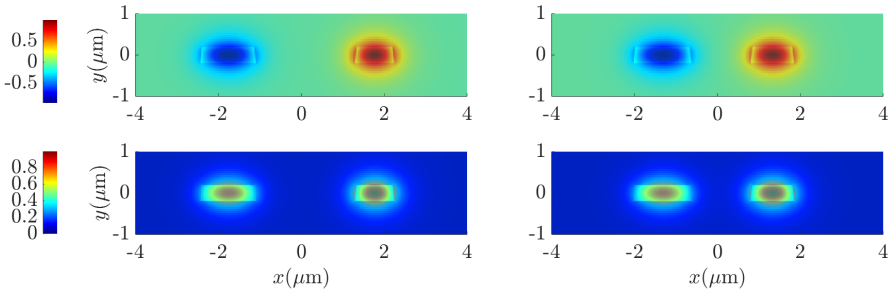


Fig. 4 Mode profiles of the supermodes of both designs. The first row shows the antisymmetric modes with clear opposite phases for the separate waveguide field profiles; the second row shows the symmetric mode with similar phases in both waveguides.

Figure 4 shows supermodes having near-identical power profiles near the AMC region but different parities of the field. We also observe the AMC in the n_{eff} plot as they deflect at the point where the uncoupled resonators cross ($\lambda = 1.55\,\mu$m).

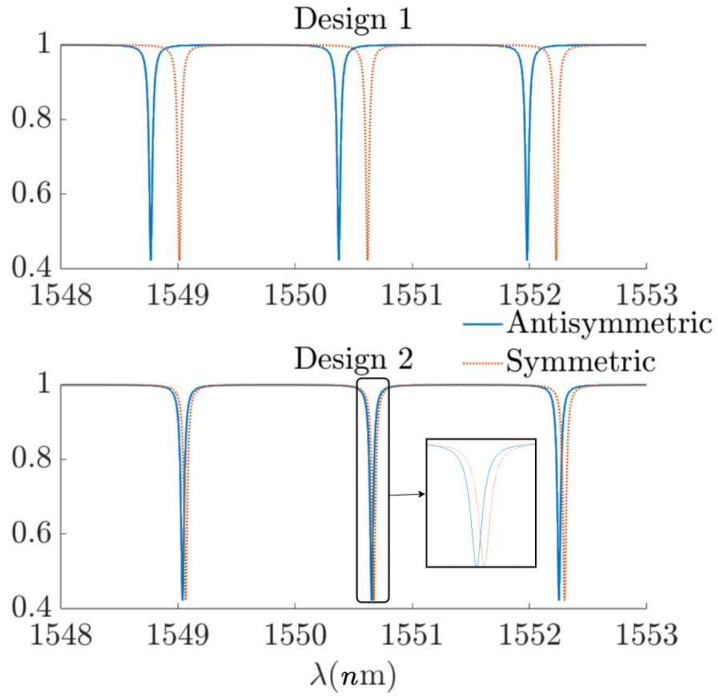


Fig. 5 The transfer function of the two designs at an arbitrary coupling coefficient, showing how the resonance frequencies are split, with the split being much smaller in design 2.

Figure 5 shows the cavity resonances around the AMC point. The splitting of the resonance frequencies for design 2 is much smaller compared to design 1. This can be explained using the coupled mode theory [25].

$$\omega_{s,as} = \frac{\omega_1 + \omega_2}{2} \pm \sqrt{\left(\frac{\omega_1 - \omega_2}{2}\right)^2 + \frac{\kappa_{oi}^2}{4}} \tag{5}$$

where $\omega_{s,as}$ are the resonance frequencies of the symmetric and antisymmetric supermodes, ω_1 and ω_2 are the uncoupled resonances, and κ_{oi} is the coupling coefficient between the two concentric rings. At $\omega_1 = \omega_2$, we can predict that the design with the larger kappa (smaller Δ_r) has a larger splitting.

3 Intermodal Coupling

The supermodes of the concentric ring structure are the orthogonal eigenmodes of the structure. However, the presence of the coupler creates a perturbation to this orthogonality and results in power exchange between them (see Fig. 6) with a power coupling coefficient T_{IM}.

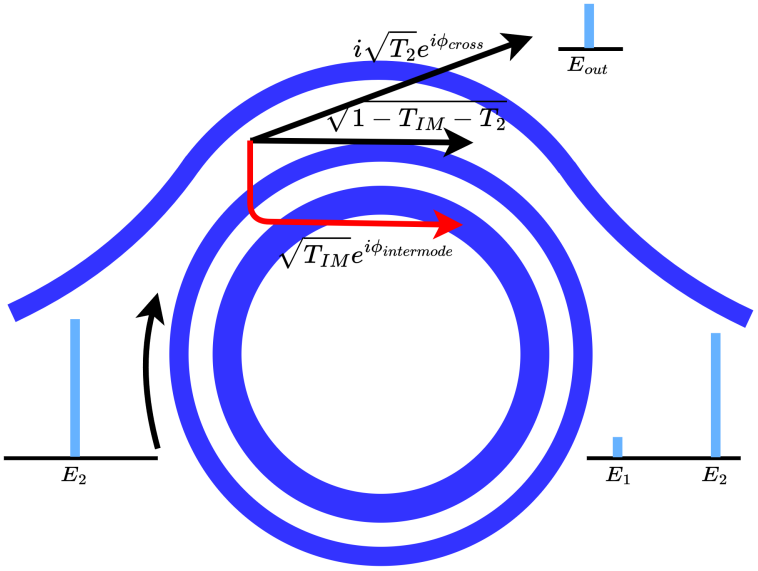


Fig. 6 Illustration of the intermodal coupling produced in the concentric rings, showing how part of the field of antisymmetric supermode 2 couples to symmetric supermode 1 after passing by the coupler (the same behavior occurs when mode 1 is excited).

At the AMC region, the difference in the effective indices between the supermodes of both designs is on the order of 10^{-5} to 10^{-4}, and the intensity distribution of both modes is similar at the gap between the bus waveguide and the concentric rings. Therefore, nearly equal coupling strengths from the bus waveguide to both supermodes occur, as shown in Fig. 7.

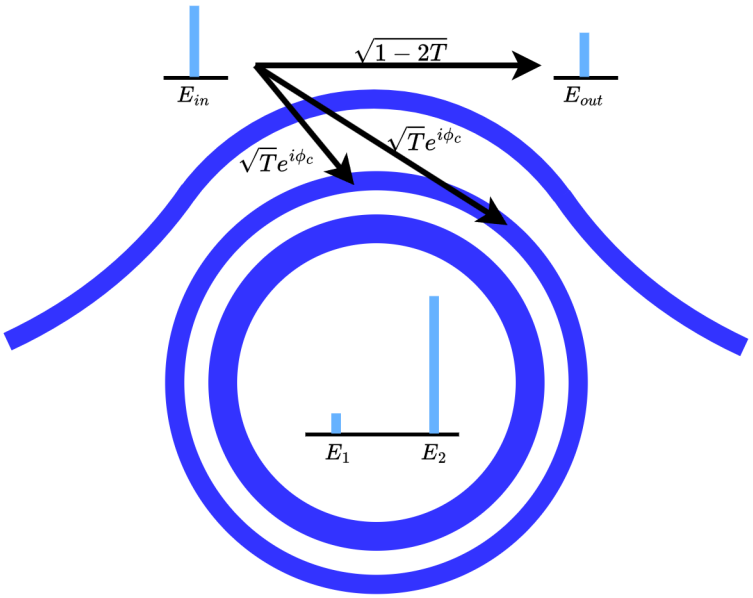


Fig. 7 Illustration of the coupling near a resonance of supermode 2 showing equal coupling to both supermodes due to near exact power profile and effective indices, but higher buildup in mode 2 due to the resonance.

Therefore, due to intermodal coupling, the directional coupler region can be modeled as a six-port network as shown in Fig. 8, with the bus fundamental mode, the symmetric mode (mode 1), and the antisymmetric mode (mode 2) on both sides identified as the six ports. The system can thus be described by a 6×6 S-parameter matrix [26, 27].

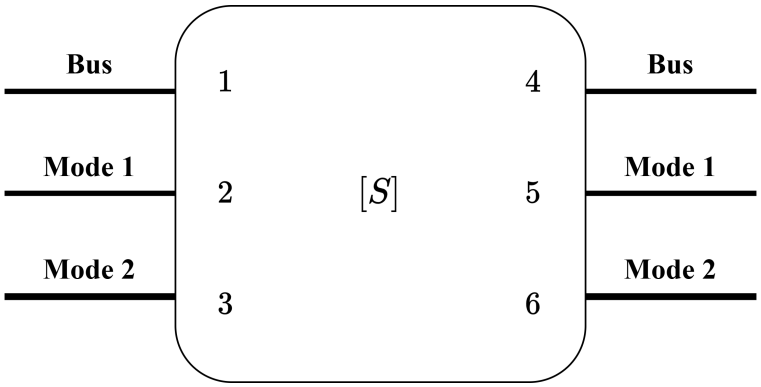


Fig. 8 Illustration of a six-port network in the coupling point.

As the system is reciprocal, $S_{ij} = S_{ji}$, and we assume all the ports to be matched with no reflection, which gives $S_{ii} = 0$. This reduces the matrix to:

$$\begin{bmatrix} 0 & 0 & 0 & S_{41} & S_{51} & S_{61} \\ 0 & 0 & 0 & S_{42} & S_{52} & S_{62} \\ 0 & 0 & 0 & S_{43} & S_{53} & S_{63} \\ S_{41} & S_{42} & S_{43} & 0 & 0 & 0 \\ S_{51} & S_{52} & S_{53} & 0 & 0 & 0 \\ S_{61} & S_{62} & S_{63} & 0 & 0 & 0 \end{bmatrix} = \begin{bmatrix} \mathbf{0} & [\mathbf{M}_1]^T \\ [\mathbf{M}_1] & \mathbf{0} \end{bmatrix} \tag{6}$$

In addition, we assume in our analysis that the system is lossless and normalize the phases so that any through transmission has a phase of zero, which gives:

$$\mathbf{M}_1 = \begin{bmatrix} \sqrt{1-2T} & \sqrt{T}e^{i\phi_c} & \sqrt{T}e^{i\phi_c} \\ \sqrt{T}e^{i\phi_c} & \sqrt{1-T_{\mathrm{IM}}-T} & \sqrt{T_{\mathrm{IM}}}e^{i\phi_{\mathrm{im}}} \\ \sqrt{T}e^{i\phi_c} & \sqrt{T_{\mathrm{IM}}}e^{i\phi_{\mathrm{im}}} & \sqrt{1-T_{\mathrm{IM}}-T} \end{bmatrix}$$

Here, $\phi_{\mathrm{im}(c)}$ indicates $\phi_{\mathrm{intermode(cross)}}$, and the lossless condition is:

$$\sum_i S_{ij} S_{ik}^* = 0, \qquad j \neq k \tag{7}$$

We then get two equations describing the phase terms:

$$\phi_{\mathrm{im}} = \cos^{-1} \frac{-T}{2\sqrt{T_{\mathrm{IM}}\left(1 - T_{\mathrm{IM}} - T\right)}} \tag{8}$$

and

$$\phi_c = -\frac{i}{2} \ln\left(\frac{-\sqrt{1-2T}}{\sqrt{1-T_{\mathrm{IM}}-T} + \sqrt{T_{\mathrm{IM}}}\, e^{-i\phi_{\mathrm{im}}}} \right) \tag{9}$$

Based on the Ikeda map of a propagating cavity mode coupled to the coupler once per round-trip [17, 24, 28, 29], the evolution of the propagating mode in the resonator can be described by:

$$\frac{\partial A}{\partial z} = -\left(\frac{\alpha_i}{2} + i\delta\right) A - \sum_{n=2}^{\infty} i^{n-1} \frac{\beta_n}{n!} \frac{\partial^n A}{\partial t^n} + i\gamma |A|^2 A \tag{10}$$

where A is the mode slowly varying envelope, $\gamma = \frac{\omega_0 n_2}{c A_{\mathrm{eff}}}$ is the nonlinear coefficient, ω_0 is the central angular frequency, n_2 is the nonlinear refractive index, c is the speed of light in free space, and A_{eff} is the effective mode area. $\beta_n = \frac{d^n \beta}{d\omega^n}$ is the group velocity dispersion term. It is calculated at the center angular frequency. The boundary condition for the intracavity field at the coupling point is given as:

$$A^{(m+1)}(0,t) = \sqrt{1-T}\, A^{(m)}(L,t) + \sqrt{T} A_{\mathrm{in}} \tag{11}$$

where m is the round-trip index. Applying Eq. (10) to the two supermodes of the resonator, taking into account nonlinear coupling between the two modes via cross-phase modulation (XPM), we get the following coupled Ikeda maps model:

$$\frac{\partial A_2}{\partial z} = -\left(\frac{\alpha_i}{2} + i\delta\right) A_2 - \sum_{n=2}^{\infty} i^{n-1} \frac{\beta_n^{(2)}}{n!} \frac{\partial^n A_2}{\partial t^n} + i\gamma \left(|A_2|^2 + 2|A_1|^2\right) A_2 \tag{12}$$

$$\begin{aligned} \frac{\partial A_1}{\partial z} = & -\left(\frac{\alpha_i}{2} + i\delta + i\Delta\beta_0^{(1)}\right) A_1 - \Delta\beta_1^{(1)} \frac{\partial A_1}{\partial t} \\ & - \sum_{n=2}^{\infty} i^{n-1} \frac{\beta_n^{(1)}}{n!} \frac{\partial^n A_1}{\partial t^n} + i\gamma \left(|A_1|^2 + 2|A_2|^2\right) A_1 \end{aligned} \tag{13}$$

where the superscripts (1) and (2) refer to the supermode index. The XPM effect appears in the added nonlinear terms in Eqs. (12) and (13). In our analysis, we are primarily concerned with mode 2 (antisymmetric supermode). The superscript ($v = 1$ and 2) identifies supermode 1 ($v = 1$) and supermode 2 ($v = 2$). The retarded time in our model evolves with its group velocity, resulting in the terms $\Delta\beta_0^{(1)} = \beta_0^{(1)} - \beta_0^{(2)}$ and $\Delta\beta_1^{(1)} = \beta_1^{(1)} - \beta_1^{(2)}$ in Eq. (13), which represent the intrinsic propagation constant mismatch between the two supermodes and the group velocities normalized with respect to mode 2. Based on the analysis performed on the six-port network describing the directional coupler, the equations describing the boundary conditions are:

$$A_{1,2}^{(m+1)}(0,t) = \sqrt{1 - T_{\mathrm{IM}} - T}\, A_{1,2}^{(m)}(L,t) + \sqrt{T} e^{i\phi_c} A_{\mathrm{in}} + \sqrt{T_{\mathrm{IM}}} e^{i\phi_{\mathrm{im}}} A_{2,1}^{(m)}(L,t) \tag{14}$$

$$A_{\mathrm{out}}^{(m)} = \sqrt{1 - 2T} A_{\mathrm{in}} + \sqrt{T} e^{i\phi_c} \left(A_1^{(m)}(L,t) + A_2^{(m)}(L,t)\right) \tag{15}$$

This model will be the foundation for studying the effects brought on by the intermodal coupling.

4 CW Solutions and Tristability

In the previous section we mentioned the modified boundary conditions, and now we will discuss the implications of that on the CW solutions of the concentric micro-rings. The methodology followed is close to the one followed in [22] We derive the Ikeda map steady state solutions via equating the field at the start of each round-trip for both modes:

$$A_{1,2}^{(m+1)}(0) = A_{1,2}^{(m)}(0) = A_{1,2}^{\mathrm{ss}} \tag{16}$$

taking the field at the end of each roundtrip to be

$$A_{1,2}(L) = A_{1,2}^{\mathrm{ss}} \exp\left(-(\frac{\alpha_i}{2} + i\delta_{1,2})L + \gamma L_{\mathrm{eff}}(|A_{1,2}|^2 + 2\,|A_{2,1}|^2)\right) = A_{1,2}^{\mathrm{ss}} Q_{1,2} \tag{17}$$

$L_{\text{eff}} = (1 - e^{-\alpha_i L})/\alpha_i$being the effective length of the nonlinearity, resulting in the 2 equations(1 for each supermode) for the steady-state:

$$A_{1,2}^{\text{ss}} = \sqrt{1 - T_{\text{IM}} - T}\, A_{1,2}^{\text{ss}} Q_{1,2} + \sqrt{T} e^{i\phi_c} A_{\text{in}} + \sqrt{T_{\text{IM}}} e^{i\phi_{\text{im}}} A_{2,1}^{\text{ss}} Q_{2,1} \tag{18}$$

These 2 equations do not offer an analytical solution due to the XPM terms in the exponential and we solve this system numerically via a branch continuation method [30, 31]

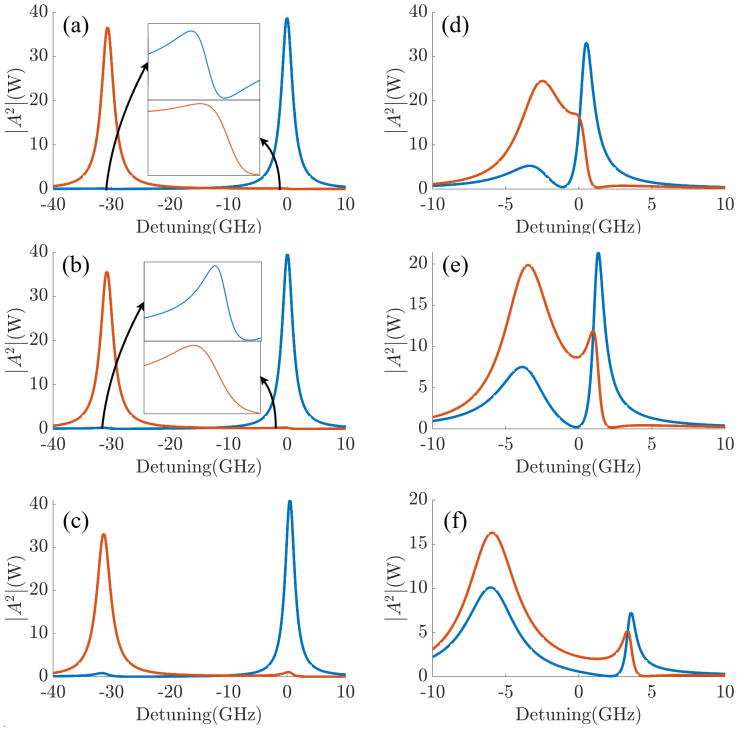


Fig. 9 Linear cavity ($\gamma = 0$) CW solutions (red (dashed) for mode 1, blue (solid) for mode 2) for $T_{\text{im}} = 0.002, 0.005, 0.02$ for rows 1,2,3 respectively and input power 1W. (a),(b),(c) are for design 1 with $\Delta\beta_0 L = 0.955$rad corresponding to a 30GHz shift between the mode resonances and (d),(e),(f) are for design 2 with $\Delta\beta_0 L = 0.07$rad corresponding to a 2.25GHz shift between the mode resonances

To isolate the effect of intermodal coupling, in Fig.9 we set $\gamma = 0$. For both designs, we then observe smaller embedded peaks of the opposite mode inside the larger peak, proportional to the intermodal coupling term T_{IM} , the effects are also more pronounced the closer the resonances are to each other as we can see in the design 2 plots. It can be intuitive to think of each mode near its eigenfrequency as a pump for the off-resonance one, whether that pumping depletes the pump and to what extent needs further examination of the coupling coefficients for each specific case but we can

see how the deviations to the original resonance frequency would increase the larger T_{im} is from (8),(9), most cases we find the peak of mode 2 higher than that of mode 1.

Fig10 shows how In the presence of nonlinearity ($\gamma = 0.5877$ in our case) the progression of the CW solutions from a small tilt in both peaks of each mode to bistability, then tristability as we increase the power. Input powers may also seem too high, however, many presently available technologies can offer orders of magnitude lower losses, and that can reduce the power needed to reach tristability to the $\sim$ 100mW range. In our system we can achieve tristability with much lower power and nonlinear resonance shift (¡0.5π) when compared to the single ring multistability threshold that requires a nonlinear phase shift of 2π and thus much higher powers at the same Q-factor [22].

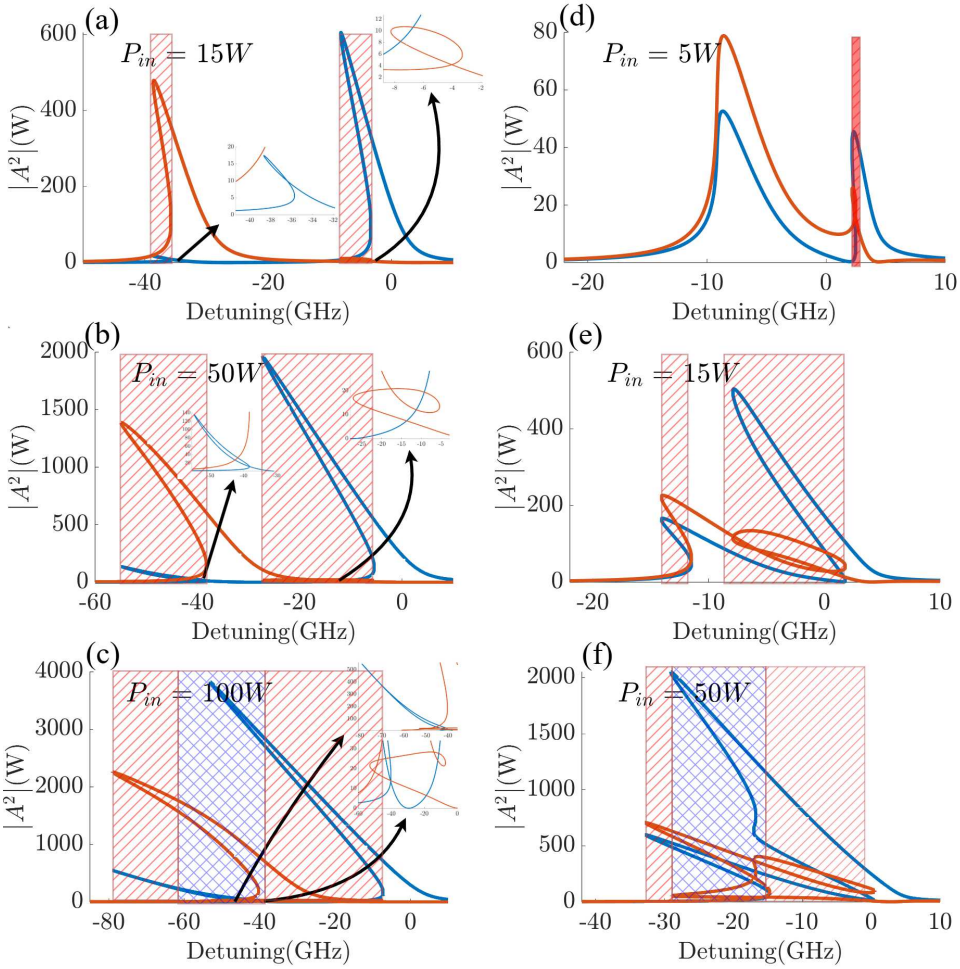


Fig. 10 Nonlinear cavity ($\gamma = 0.5877$) CW solutions (same color scheme as Fig.9) for $T_{\text{IM}} = 0.02$ at different P_{in}. a,b,c are for design 1 and d,e,f are for design 2. Red hatched region are bistable and Blue cross-hatched regions are Tristable. Insets show closer features of the smaller peaks.

We have found an interesting observation related to the peaks of the off-resonance tilted peaks visible in Fig.11, at higher pump powers, the tail of the on-resonance peak elevates the lower branch of the off-resonance peak higher than the upper branch that is pumped by the intermodal coupling. The sharp feature of the unstable branches in Figures(10,11) is due to the straight line interpolation used as our numerical methods don't converge on them.

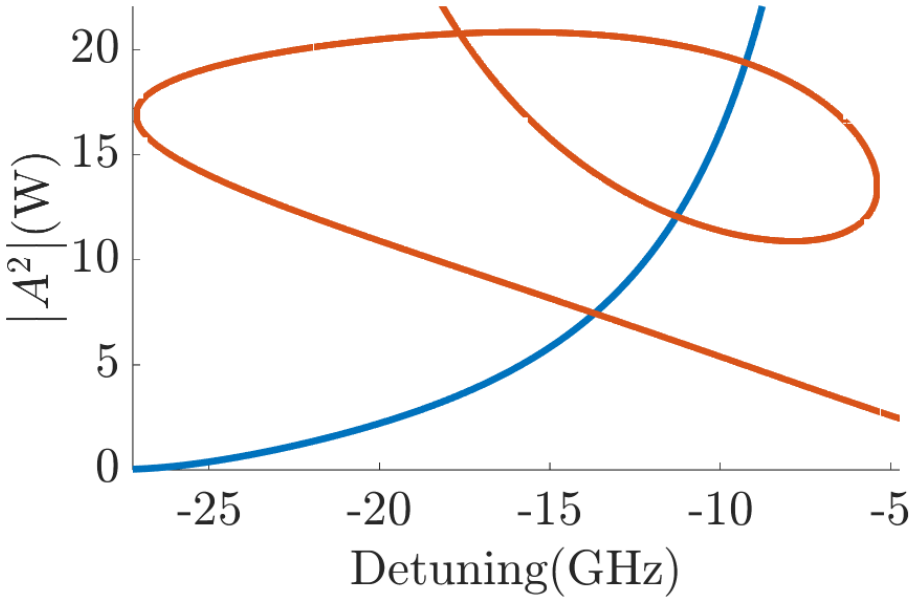


Fig. 11 Flipped peak of mode 2 off-resonance peak, same parameters as in 10.b

We also investigated the relationship between input power A_{in}^2 and intracavity power in the 2 supermodes at the detunings where Tristability is present.

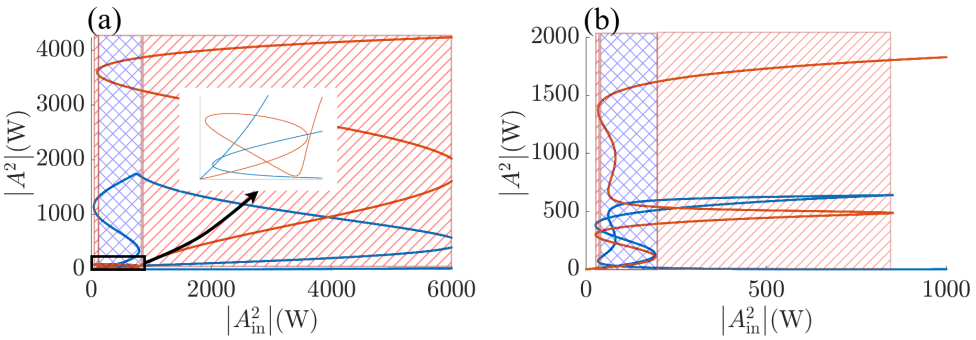


Fig. 12 (a) supermode intensites for design 1 at different input powers and at a detuning of -20GHz,(b) supermode intensites for design 2 at different input powers and at a detuning of -50GHz. Same parameters and color schemes as in 10

.

In this section we investigated the CW solutions of our system revealing tristability at relatively low nonlinear phase shift and outlined the shape of the off-resonance peaks at high powers.

5 Modulation Instability Analysis for the Concentric Ring

OFC generation in microresonators pumped by CW sources relies on the gain experienced by sidebands seeded by noise or small perturbations; in other words, on the modulational instability (MI) of the pump mode. Four-wave mixing (FWM) is responsible for the nonlinear amplification, which is highly dependent on phase matching [15–17, 24]. Unlike in a straight waveguide, a resonator provides an additional degree of freedom for phase matching through the cavity detuning [15, 16]. In addition, the resonator may exhibit MI imposed by the discrete boundary condition that is not predicted by the mean-field model and can only be captured using the Ikeda map [22].

Analyses of this nature have been performed using mean-field models based on the Lugiato–Lefever equation (LLE) [15, 16, 32]. However, the LLE does not capture the complete discrete round-trip dynamics of the system. The Ikeda map can capture a broader range of dynamics, including period-doubled solutions and multiple instability tongues corresponding to distinct unstable frequency bands [22].

To investigate the stability of equations (12)–(14), we write the fields as

$$\begin{aligned} A_1^{(m)}(z,t) &= \left[A_1^{\text{ss}} e^{-\alpha_i z/2} + u_1^{(m)}(z,t) + i v_1^{(m)}(z,t)\right] e^{i\phi_1(z)}, \\ A_2^{(m)}(z,t) &= \left[A_2^{\text{ss}} e^{-\alpha_i z/2} + u_2^{(m)}(z,t) + i v_2^{(m)}(z,t)\right] e^{i\phi_2(z)}, \end{aligned} \tag{19}$$

where

$$\phi_1(z) = \gamma \left(\frac{1 - e^{-\alpha_i z}}{\alpha_i}\right) \left(|A_1^{\text{ss}}|^2 + 2\,|A_2^{\text{ss}}|^2\right), \tag{20}$$

and

$$\phi_2(z) = \gamma \left(\frac{1 - e^{-\alpha_i z}}{\alpha_i} \right) \left(|A_2^{\mathrm{ss}}|^2 + 2\,|A_1^{\mathrm{ss}}|^2 \right). \tag{21}$$

Here, $u_{1,2}(z,t)$ and $v_{1,2}(z,t)$ are real functions representing small physical perturbations in modes 1 and 2, respectively. The propagation loss of the perturbations is retained explicitly in the linearized equations.

After linearizing the coupled NLSEs and Fourier transforming with respect to the fast time t, we define the perturbation vector

$$\mathbf{w}^{(m)}(z) = \begin{bmatrix} \tilde{u}_1^{(m)}(\omega, z) \\ \tilde{v}_1^{(m)}(\omega, z) \\ \tilde{u}_2^{(m)}(\omega, z) \\ \tilde{v}_2^{(m)}(\omega, z) \end{bmatrix}, \tag{22}$$

which satisfies

$$\frac{d\mathbf{w}^{(m)}}{dz} = \mathbf{M}(z, \omega)\mathbf{w}^{(m)}. \tag{23}$$

Assuming that the perturbation quadratures are defined relative to the phases of the corresponding steady-state fields, the perturbation matrix is

$$\mathbf{M}(z,\omega) = \begin{bmatrix} -\dfrac{\alpha_i}{2} & -\dfrac{\beta_2^{(1)}}{2}\omega^2 & 0 & 0 \\ \dfrac{\beta_2^{(1)}}{2}\omega^2 + 2\gamma\,|A_1|^2\,e^{-\alpha_i z} & -\dfrac{\alpha_i}{2} & 4\gamma\,|A_1|\,|A_2|\,e^{-\alpha_i z} & 0 \\ 0 & 0 & -\dfrac{\alpha_i}{2} & -\dfrac{\beta_2^{(2)}}{2}\omega^2 \\ 4\gamma\,|A_1|\,|A_2|\,e^{-\alpha_i z} & 0 & \dfrac{\beta_2^{(2)}}{2}\omega^2 + 2\gamma\,|A_2|^2\,e^{-\alpha_i z} & -\dfrac{\alpha_i}{2} \end{bmatrix}. \tag{24}$$

The diagonal terms $-\alpha_i/2$ account for the amplitude loss experienced by the perturbations during propagation. The factors $e^{-\alpha_i z}$ in the nonlinear coefficients account for the decay of the local CW powers along the ring. The terms proportional to $4\gamma|A_1||A_2|$ arise from the linearization of the cross-phase-modulation terms and couple the perturbations of the two modes.

The matrix is integrated over the cavity round-trip length. The phase shifts and boundary conditions are then applied to obtain the perturbation state at the beginning of the next round trip. The total phase rotations are defined as

$$\delta_1 = \phi_1(L) - \delta_{0,1}, \qquad \delta_2 = \phi_2(L) - \delta_{0,2}, \tag{25}$$

where $\delta_{0,1}$ and $\delta_{0,2}$ are the linear cavity detunings. This sign corresponds to a boundary-condition convention containing $e^{-i\delta_{0,j}}$. If the opposite convention is used in equations (12)–(14), the signs of the linear detunings must be reversed.

The corresponding quadrature rotation matrix is

$$\mathbf{R}_\phi = \begin{bmatrix} \cos(\delta_1) & -\sin(\delta_1) & 0 & 0 \\ \sin(\delta_1) & \cos(\delta_1) & 0 & 0 \\ 0 & 0 & \cos(\delta_2) & -\sin(\delta_2) \\ 0 & 0 & \sin(\delta_2) & \cos(\delta_2) \end{bmatrix}. \tag{26}$$

The nonlinear phases $\phi_1(L)$ and $\phi_2(L)$ are included only through δ_1 and δ_2. The nonlinear terms in $\mathbf{M}$ describe the evolution of the perturbations relative to the CW background and therefore do not constitute a second application of the common nonlinear phase.

The intermodal coupling at the coupler is represented by

$$\mathbf{T}_{\mathrm{IM}} = \begin{bmatrix} 0 & 0 & \mathrm{Re}(\tau_{\mathrm{im}}) & -\mathrm{Im}(\tau_{\mathrm{im}}) \\ 0 & 0 & \mathrm{Im}(\tau_{\mathrm{im}}) & \mathrm{Re}(\tau_{\mathrm{im}}) \\ \mathrm{Re}(\tau_{\mathrm{im}}) & -\mathrm{Im}(\tau_{\mathrm{im}}) & 0 & 0 \\ \mathrm{Im}(\tau_{\mathrm{im}}) & \mathrm{Re}(\tau_{\mathrm{im}}) & 0 & 0 \end{bmatrix}, \tag{27}$$

where

$$\tau_{\mathrm{im}} = \sqrt{T_{\mathrm{IM}}}\, e^{i\phi_{\mathrm{im}}}. \tag{28}$$

The stability of the system is investigated numerically using Floquet analysis. Four independent initial perturbations are used:

$$\mathbf{w}_1(0) = \begin{bmatrix} 1 \\ 0 \\ 0 \\ 0 \end{bmatrix}, \qquad \mathbf{w}_2(0) = \begin{bmatrix} 0 \\ 1 \\ 0 \\ 0 \end{bmatrix}, \qquad \mathbf{w}_3(0) = \begin{bmatrix} 0 \\ 0 \\ 1 \\ 0 \end{bmatrix}, \qquad \mathbf{w}_4(0) = \begin{bmatrix} 0 \\ 0 \\ 0 \\ 1 \end{bmatrix}. \tag{29}$$

Each initial condition is propagated independently from $z = 0$ to $z = L$. The cavity phase rotation and boundary coupling are then applied according to

$$\mathbf{w}^{(m+1)}(0) = (\tau\mathbf{I} + \mathbf{T}_{\mathrm{IM}})\, \mathbf{R}_\phi \mathbf{w}^{(m)}(L), \tag{30}$$

where

$$\tau = \sqrt{1 - T_{\mathrm{IM}} - T}. \tag{31}$$

No additional propagation-loss factor is applied in equation (30), since the distributed propagation loss is already included in the diagonal entries of $\mathbf{M}$.

The four resulting perturbation vectors form the columns of the monodromy matrix [22]:

$$\mathbf{\Phi}(\omega) = \left[\mathbf{w}_1^{(m+1)}(0)\ \mathbf{w}_2^{(m+1)}(0)\ \mathbf{w}_3^{(m+1)}(0)\ \mathbf{w}_4^{(m+1)}(0)\right]. \tag{32}$$

The eigenvalues of $\mathbf{\Phi}$ are the Floquet multipliers. The system is unstable when at least one multiplier satisfies

$$|\lambda_j| > 1. \tag{33}$$

The maximum round-trip MI gain is therefore defined as

$$g(\omega) = \max_j \left[\ln |\lambda_j(\omega)|\right]. \tag{34}$$

The perturbation matrix depends on the intracavity amplitudes of the two modes, the perturbation frequency ω, or equivalently the resonator mode order μ, and the two cavity detunings. We run our Floquet analysis on our CW plots to find the regions with MI, We iterate over a large number mode orders to check if any of them experience any MI gain.

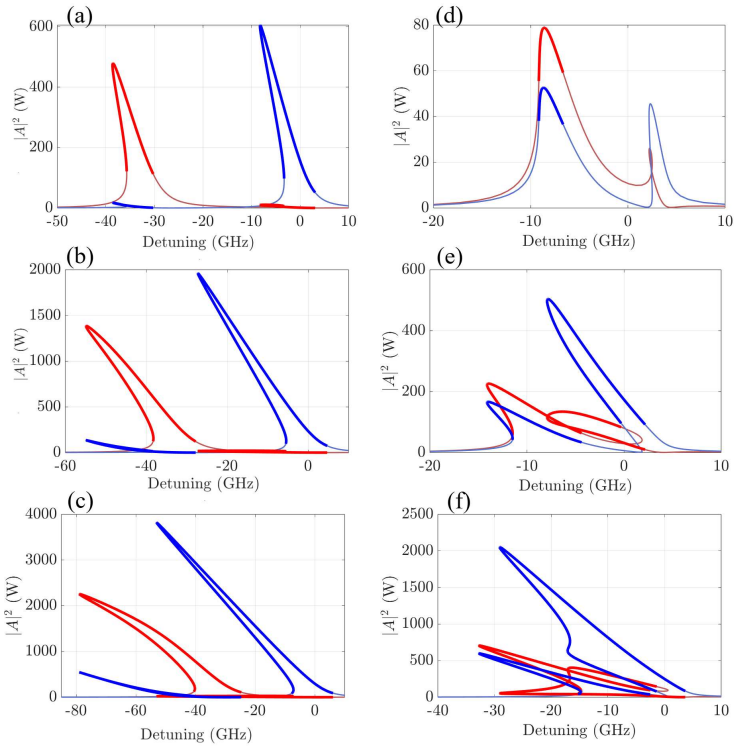


Fig. 13 Highlighted unstable values, showing where the MI starts. It is superimposed on the plots of the variation of the supermode intracavity power with input power at the same detuning in fig.10

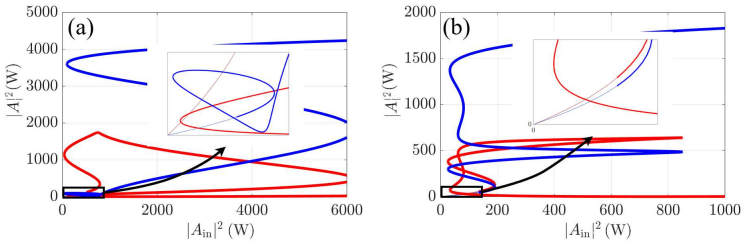


Fig. 14 Highlighted unstable values, showing where the MI starts. It is superimposed on the plots of the nonlinear cavity CW solutions in as in fig.12

In this section we outlined the regions of MI for our Ikeda map model and explored two ways of visualizing regions with MI. Both visualizations carry a great benefit to any simulation or experimental setup.

6 Ikeda map results

In this section we simulate the model we derived in Section 3. Our method of simulation is using the split-step fast Fourier transform(SS-FFT)method[17, 33–35]. We scanned the detuning(from higher to lower frequencies) at a constant pump power. We investigate the evolution of the fields of both modes, it is also worth noting that our results can vary significantly with how we choose our initial detuning value which in turn will influence which branch we will follow for the portion of our detuning sweep that has a CW solution Fig.10. We restrict the simulation results to cases with a single soliton solution.

For design 1 we obtain a single cavity soliton at relatively lower powers and the results do not vary much from the ones predicted without the intermodal coupling Fig.15. This can be attributed to a clear feature in Fig.10, which is that the off-resonance peaks are rather small. We perform a detuning sweep at 6W of input power around the Antisymmetric on-resonance peak, we observe that the power accumulated in the symmetric mode is not enough for it to display any emergent dynamics and remains mostly an attenuated picture of the antisymmetric mode. There is some modulation in the spectrum resembling a dark soliton however not strong enough to reflect in the temporal shape.

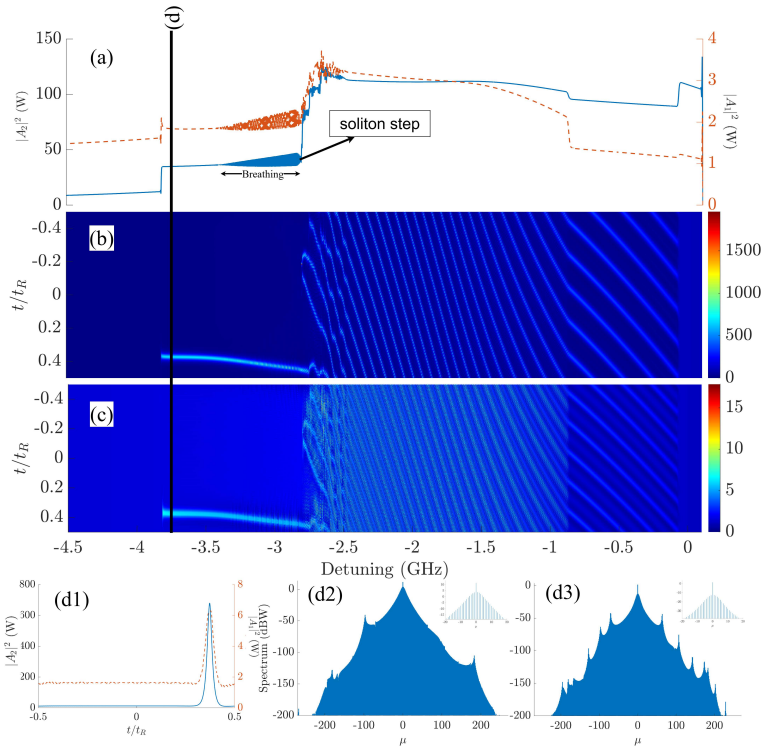


Fig. 15 (a)Intracavity power in super modes 1 and 2 plotted against detuning. Note the following features: the soliton step, the difference in powers between modes, and decrease in soliton power oscillations(breathing when detuning further) around point(d). (b)and(c) The trace of the intracavity temporal envelope against detuning for super modes 2,1. (d1) The intracavity power envelope in a span of a single roundtrip at point (d) for both modes.(d2),(d3) Spectra of super mode 2 and mode 1 at the same point showing a zoomed-in insert showing a frequency comb with single FSR spaced lines. For the coupling coefficients the parameters are $T = 0.05, T_{\mathrm{IM}} = 0.02$ and $P_{\mathrm{in}} = 6\mathrm{W}$

For design 2 the intermodal buildup is much more apparent as we can see in Figs.9 and 10, this also appears in the results of our sweeps where we observe emergent dynamics in the off-resonant symmetric mode with normal dispersion. We observe co-propagating bright-dark soliton states with a bright soliton in the antisymmetric mode and a dark soliton in the symmetric mode existing in the same position in the cavity Fig.16(d1). This effect is most pronounced during the breathing phase in our sweep, where the stronger bright solitons "lock" with the more pronounced dark solitons, this effect is largely attributed to XPM, and carries a strong resemblance to the results found in [36] with dual pumped cavities in different dispersion regimes. This effect provides similar benefits to the mode-locking of the OFC however, it relies on a single pump frequency and the intermodal coupling of the concentric cavity.

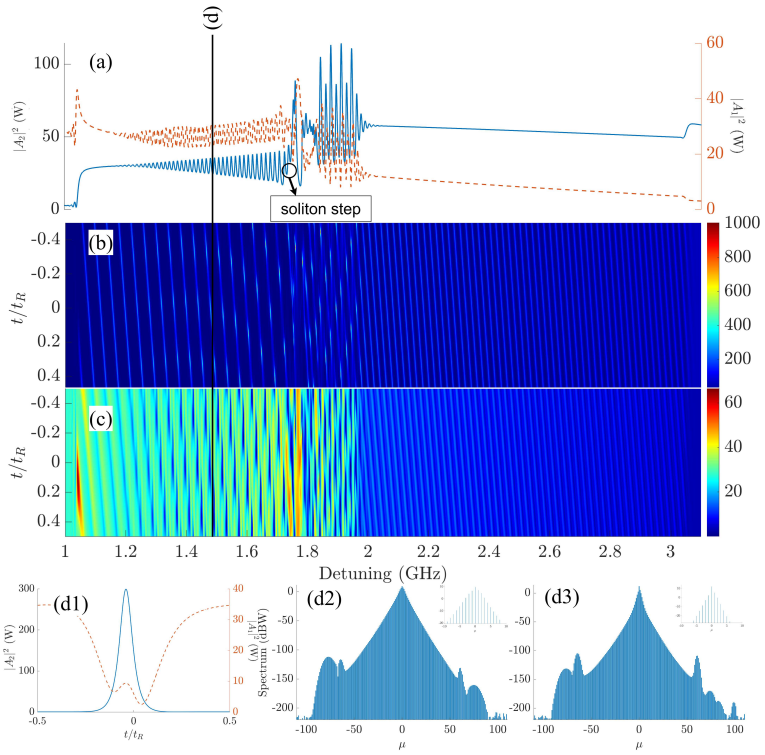


Fig. 16 Detuning sweep of design 2 at $P_{\text{in}} = 15$W. The graph labels, coupling parameters and color schemes are the same as in Fig.15

7 Conclusion

In this work, we demonstrated a method to achieve anomalous dispersion in Si_3N_4 concentric microrings at a targeted FSR and identified a previously unreported intermodal coupling effect at the coupling point. By incorporating this effect into the boundary conditions via an Scattering matrix analysis, we extended the Ikeda map model to more accurately describe the intracavity dynamics. Using this framework, we showed that the CW response transitions from bistability to tristability at relatively low nonlinear phase shifts, suggesting potential for optical memory and computational applications. Numerical investigation of modulation instability further revealed dynamics that deviate significantly from mean-field and Ikeda models that don't account for this coupling, including the emergence of co-propagating bright?dark soliton states mediated by intermodal cross-phase modulation. These findings establish concentric microrings as a versatile platform for studying nonlinear dynamics beyond

conventional models. Future work will explore the stability of tristable states and the role of modulation instability in shaping soliton generation.

Declarations

The author(s) received no financial support for the research, authorship, and/or publication of this article.

References

[1] Kippenberg, T.J., Holzwarth, R., Diddams, S.A.: Microresonator-based optical frequency combs. Science **332**(6029), 555–559 (2011) https://doi.org/10.1126/science.1193968 https://www.science.org/doi/pdf/10.1126/science.1193968

[2] Steinmetz, T., Wilken, T., Araujo-Hauck, C., Holzwarth, R., Hänsch, T.W., Pasquini, L., Manescau, A., D'Odorico, S., Murphy, M.T., Kentischer, T., Schmidt, W., Udem, T.: Laser frequency combs for astronomical observations. Science **321**(5894), 1335–1337 (2008) https://doi.org/10.1126/science.1161030 https://www.science.org/doi/pdf/10.1126/science.1161030

[3] Suh, M.-G., Vahala, K.J.: Soliton microcomb range measurement. Science **359**(6378), 884–887 (2018) https://doi.org/10.1126/science.aao1968 https://www.science.org/doi/pdf/10.1126/science.aao1968

[4] Spencer, D.T., Drake, T., Briles, T.C., Stone, J., Sinclair, L.C., Fredrick, C., Li, Q., Westly, D., Ilic, B.R., Bluestone, A., Volet, N., Komljenovic, T., Chang, L., Lee, S.H., Oh, D.Y., Suh, M.-G., Yang, K.Y., Pfeiffer, M.H.P., Kippenberg, T.J., Norberg, E., Theogarajan, L., Vahala, K., Newbury, N.R., Srinivasan, K., Bowers, J.E., Diddams, S.A., Papp, S.B.: An optical-frequency synthesizer using integrated photonics. Nature **557**(7703), 81–85 (2018) https://doi.org/10.1038/s41586-018-0065-7

[5] Picqué, N., Hänsch, T.W.: Frequency comb spectroscopy. Nature Photonics **13**(3), 146–157 (2019) https://doi.org/10.1038/s41566-018-0347-5

[6] Marin-Palomo, P., Kemal, J.N., Karpov, M., Kordts, A., Pfeifle, J., Pfeiffer, M.H.P., Trocha, P., Wolf, S., Brasch, V., Anderson, M.H., Rosenberger, R., Vijayan, K., Freude, W., Kippenberg, T.J., Koos, C.: Microresonator-based solitons for massively parallel coherent optical communications. Nature **546**(7657), 274–279 (2017) https://doi.org/10.1038/nature22387

[7] Gupta, R., Kumar, A., Kumar, M., Singh, R., Gehlot, A., Pandey, P.S., Yadav, N., Pandey, K., Yadav, A., Gupta, N., Brajpuriya, R., Kumar, S., Verma, A.S., Kumar, T., Wu, Y., Hongyu, Z., Biswas, A., Mittal, A., Mondal, A., Ivanovich, R.O.: The integration of microelectronic and photonic circuits on a single silicon chip for high-speed and low-power optoelectronic technology. Nano Materials Science **7**(3), 305–315 (2025) https://doi.org/10.1016/j.nanoms.2024.04.011

[8] Moss, D.J., Morandotti, R., Gaeta, A.L., Lipson, M.: New cmos-compatible platforms based on silicon nitride and hydex for nonlinear optics. Nature Photonics **7**(8), 597–607 (2013) https://doi.org/10.1038/nphoton.2013.183

[9] Doerr, C.R.: Silicon photonic integration in telecommunications. Frontiers in Physics **Volume 3 - 2015** (2015) https://doi.org/10.3389/fphy.2015.00037

[10] Liu, J., Huang, G., Wang, R.N., He, J., Raja, A.S., Liu, T., Engelsen, N.J., Kippenberg, T.J.: High-yield, wafer-scale fabrication of ultralow-loss, dispersion-engineered silicon nitride photonic circuits. Nature Communications **12**(1), 2236 (2021) https://doi.org/10.1038/s41467-021-21973-z

[11] Torres-Company, V., Castelló-Lurbe, D., Silvestre, E.: Comparative analysis of spectral coherence in microresonator frequency combs. Opt. Express **22**(4), 4678–4691 (2014) https://doi.org/10.1364/OE.22.004678

[12] Chang, L., Xie, W., Shu, H., Yang, Q.-F., Shen, B., Boes, A., Peters, J.D., Jin, W., Xiang, C., Liu, S., Moille, G., Yu, S.-P., Wang, X., Srinivasan, K., Papp, S.B., Vahala, K., Bowers, J.E.: Ultra-efficient frequency comb generation in algaas-on-insulator microresonators. Nature Communications **11**(1), 1331 (2020) https://doi.org/10.1038/s41467-020-15005-5

[13] Xie, W., Chang, L., Shu, H., Norman, J.C., Peters, J.D., Wang, X., Bowers, J.E.: Ultrahigh-q algaas-on-insulator microresonators for integrated nonlinear photonics. Opt. Express **28**(22), 32894–32906 (2020) https://doi.org/10.1364/OE.405343

[14] Xuan, Y., Liu, Y., Varghese, L.T., Metcalf, A.J., Xue, X., Wang, P.-H., Han, K., Jaramillo-Villegas, J.A., Noman, A.A., Wang, C., Kim, S., Teng, M., Lee, Y.J., Niu, B., Fan, L., Wang, J., Leaird, D.E., Weiner, A.M., Qi, M.: High-q silicon nitride microresonators exhibiting low-power frequency comb initiation. Optica **3**(11), 1171–1180 (2016) https://doi.org/10.1364/OPTICA.3.001171

[15] Chembo, Y.K., Yu, N.: Modal expansion approach to optical-frequency-comb generation with monolithic whispering-gallery-mode resonators. Phys. Rev. A **82**, 033801 (2010) https://doi.org/10.1103/PhysRevA.82.033801

[16] Godey, C., Balakireva, I.V., Coillet, A., Chembo, Y.K.: Stability analysis of the spatiotemporal lugiato-lefever model for kerr optical frequency combs in the anomalous and normal dispersion regimes. Phys. Rev. A **89**, 063814 (2014) https://doi.org/10.1103/PhysRevA.89.063814

[17] Agrawal, G.P.: Chapter 5 - optical solitons. In: Agrawal, G. (ed.) Nonlinear Fiber Optics (Fifth Edition), Fifth edition edn. Optics and Photonics, pp. 129–191. Academic Press, Boston (2013). https://doi.org/10.1016/B978-0-12-397023-7.00005-X . https://www.sciencedirect.com/science/article/pii/B978012397023700005X

[18] Kim, S., Han, K., Wang, C., Jaramillo-Villegas, J.A., Xue, X., Bao, C., Xuan, Y., Leaird, D.E., Weiner, A.M., Qi, M.: Dispersion engineering and frequency comb generation in thin silicon nitride concentric microresonators. Nature Communications **8**(1), 372 (2017) https://doi.org/10.1038/s41467-017-00491-x

[19] Miller, S.A., Okawachi, Y., Ramelow, S., Luke, K., Dutt, A., Farsi, A., Gaeta, A.L., Lipson, M.: Tunable frequency combs based on dual microring resonators. Opt. Express **23**(16), 21527–21540 (2015) https://doi.org/10.1364/OE.23.021527

[20] Hansson, T., Modotto, D., Wabnitz, S.: On the numerical simulation of kerr frequency combs using coupled mode equations. Optics Communications **312**, 134–136 (2014) https://doi.org/10.1016/j.optcom.2013.09.017

[21] Ikeda, K.: Multiple-valued stationary state and its instability of the transmitted light by a ring cavity system. Optics Communications **30**(2), 257–261 (1979) https://doi.org/10.1016/0030-4018(79)90090-7

[22] Hansson, T., Wabnitz, S.: Frequency comb generation beyond the lugiato lefever equation: multi-stability and super cavity solitons. J. Opt. Soc. Am. B **32**(7), 1259–1266 (2015) https://doi.org/10.1364/JOSAB.32.001259

[23] Anderson, M., Wang, Y., Leo, F.m.c., Coen, S., Erkintalo, M., Murdoch, S.G.: Coexistence of multiple nonlinear states in a tristable passive kerr resonator. Phys. Rev. X **7**, 031031 (2017) https://doi.org/10.1103/PhysRevX.7.031031

[24] Fujii, S., Tanabe, T.: Dispersion engineering and measurement of whispering gallery mode microresonator for kerr frequency comb generation. Nanophotonics **9**(5), 1087–1104 (2020) https://doi.org/10.1515/nanoph-2019-0497

[25] Huang, W.-P.: Coupled-mode theory for optical waveguides: an overview. J. Opt. Soc. Am. A **11**(3), 963–983 (1994) https://doi.org/10.1364/JOSAA.11.000963

[26] Spagnolo, N., Aparo, L., Vitelli, C., Crespi, A., Ramponi, R., Osellame, R., Mataloni, P., Sciarrino, F.: Quantum interferometry with three-dimensional geometry. Scientific Reports **2**(1), 862 (2012) https://doi.org/10.1038/srep00862

[27] Weihs, G., Reck, M., Weinfurter, H., Zeilinger, A.: All-fiber three-path mach–zehnder interferometer. Opt. Lett. **21**(4), 302–304 (1996) https://doi.org/10.1364/OL.21.000302

[28] Abdelalim, M.A., Kotb, H.E., Joseph, E., Othman, A.M., Anis, H.: Experimental and numerical demonstration on the gain and power saturation of yb-doped double-clad fiber amplifiers in multiwavelength cw and ultrafast pulsed operation. IEEE Photonics Journal **10**(1), 1–12 (2018) https://doi.org/10.1109/JPHOT.2017.2780242

[29] Othman, A.M., Kotb, H.E., Abdelalim, M.A., Sabry, Y.M., Anis, H., Khalil,

D.: Numerical study of parabolic pulse generation in backward-pumped erbium-doped fiber amplifiers. IEEE Photonics Journal **14**(4), 1–8 (2022) https://doi.org/10.1109/JPHOT.2022.3195902

[30] Keller, H.B.: Numerical solution of bifurcation and nonlinear eigenvalue problems. In: Rabinowitz, P.H. (ed.) Applications of Bifurcation Theory, pp. 359–384. Academic Press, New York (1977)

[31] Allgower, E.L., Georg, K.: Numerical Continuation Methods: An Introduction. Springer Series in Computational Mathematics, vol. 13. Springer, Berlin (1990)

[32] Parra-Rivas, P., Gomila, D., Gelens, L., Knobloch, E.: Bifurcation structure of periodic patterns in the lugiato-lefever equation with anomalous dispersion. Phys. Rev. E **98**, 042212 (2018) https://doi.org/10.1103/PhysRevE.98.042212

[33] Kotb, H.E., Abdelalim, M.A., Anis, H.: An efficient semi-vectorial model for all-fiber mode-locked femtosecond lasers based on nonlinear polarization rotation. IEEE Journal of Selected Topics in Quantum Electronics **20**(5), 416–424 (2014) https://doi.org/10.1109/JSTQE.2014.2307302

[34] Kotb, H.E., Abdelalim, M.A., Anis, H.: Effect of mode locking technique on the filtering bandwidth limitation in all normal dispersion femtosecond fiber laser. In: Ramachandran, S. (ed.) Fiber Lasers XI: Technology, Systems, and Applications, vol. 8961, p. 89613. SPIE, ??? (2014). https://doi.org/10.1117/12.2038248 . International Society for Optics and Photonics. https://doi.org/10.1117/12.2038248

[35] Kotb, H., Abdelalim, M.A., Bock, K.J., Anis, H.: Peak power optimization of optical pulses using low-doped gain-medium in femtosecond fiber laser. J. Lightwave Technol. **31**(13), 2230–2236 (2013)

[36] Zhang, S., Bi, T., Ghalanos, G.N., Moroney, N.P., Del Bino, L., Del'Haye, P.: Dark-bright soliton bound states in a microresonator. Phys. Rev. Lett. **128**, 033901 (2022) https://doi.org/10.1103/PhysRevLett.128.033901